AIAA SciTech
5-9 January 2015, Kissimmee, Florida
53rd AIAA Aerospace Sciences Meeting

Linear analysis of jet-engine core noise based upon high-fidelity combustor and turbine simulations

Jeff O'Brien*, Jeonglae Kim†, and Matthias Ihme‡
Stanford University, Stanford, California, 94305

As further reductions in aircraft engine noise are realized, the relative importance of engine core noise increases. In this study, a computational framework for examining indirect core noise is proposed, consisting of a representative engine flow-path containing a model gas turbine combustor, a single-stage turbine, a converging nozzle, and free-field radiation. Combined high-fidelity and lower-order simulation techniques are used for each component of the modeled engine. Preliminary, uncoupled results from the combustor and turbine are presented as well as the nozzle-flow simulations. Particular attention is paid to the verification and performance of a linearized Euler solver for predicting the subsonic heated jet flow as well as its far-field acoustic radiation. Two relevant verification tests are shown as well as the nozzle's response to time-harmonic excitations in both the presence and absence of the mean jet flow over a range of Strouhal numbers. Future work will include coupling the simulations and a more detailed analysis of the mechanisms of core-noise generation and propagation.

I. Introduction

Reducing noise generated by gas-turbine engines is a major concern for engine manufacturers and the aviation industry today. Radiated sound from gas-turbine engines (such as modern turbofan engines) is often divided into several components for analysis – fan noise, compressor noise, core noise, and jet noise – with jet noise dominating the others at high-speed operating conditions. Core noise is defined as any excess noise generated within the engine core. Its generation is often associated with the combustion process and the unsteady convection of high-temperature gas,[1–3] and it is characteristically dominated by low frequencies of $O(10^2)$ Hz. Over the past several decades, significant progress has been made in reducing jet noise and fan noise, which has increased the relative importance of core noise. Furthermore, at low-speed operating conditions where jet noise is less prominent (for example, aircraft during taxi and approach, industrial gas turbines, and auxiliary power units), core noise can be significant.

Noise generated within the combustor, or direct core noise, is often reflected and scattered through the turbine stages, where it can propagate back into the combustion chamber. This can potentially trigger acoustic resonances which may lead to thermo-acoustic instabilities. In addition to direct core noise, high-temperature combustion products undergo significant acceleration while propagating through the turbine stages and exhaust nozzle, which can convert some of the entropy and vorticity fluctuations into noise. This process, often termed indirect noise,[1] can significantly impact the sound radiation of gas-turbine engines at high-speed conditions.[4,5] Since aircraft engines typically operate in this regime (due to the substantial acceleration in the turbine stages and exhaust nozzle), the indirect mechanism is likely to be the dominant source for core noise in aviation gas turbines.[1]

Understanding the fundamental mechanisms of core-noise generation and propagation is an essential step toward further reducing the overall noise from gas-turbine engines. It is also important to understand how core noise interacts with the engine components, since its generation and propagation can be closely linked with thermo-acoustic instabilities in the combustor.

*Graduate Research Assistant, Department of Mechanical Engineering.
†Post-Doctoral Fellow, Center for Turbulence Research.
‡Assistant Professor, Department of Mechanical Engineering.

While high-fidelity simulations based upon large-eddy simulation (LES) have proven useful in modeling high-speed, high-temperature turbulent flows, it is still expensive to directly apply this technique throughout the entire flow-path of gas-turbine engines. In portions of the flow-path, there is still a need to use simpler models that offer sufficiently accurate predictions at reduced computational costs, while high-fidelity simulation can be used as required where flow complexities are significant. The appropriate balance of these hybrid techniques can provide insight into the underlying mechanisms of core-noise generation and propagation at sustainable computational costs.

In this study, we investigate fundamental core-noise mechanisms in a modeled gas-turbine flow-path that contains essential components of a commercial jet engine at cruise condition. To this end, a hybrid modeling approach is used, which combines high-fidelity simulation and lower-order prediction tools. A canonical engine core is designed, consisting of a combustor, a single-stage turbine, and a converging nozzle. See *et al.*[6] studied a similar configuration without a turbine stage. The reacting flow within the combustor is modeled using LES based upon a low-Mach-number formulation of the full Navier–Stokes equations. The downstream characteristics from the combustor are then fed into the turbine-stage simulation (a one-way, downstream-only coupling). The turbine stage is predicted using a fully compressible Unsteady Reynolds-Averaged Navier–Stokes (URANS) code with moving-mesh capabilities to account for the relative motion of the rotor and stator. The turbine-stage simulation predicts the evolution of the disturbances originating from the combustor, which are then used to perturb the base state of the downstream nozzle flow. A linear model is adopted to investigate the development of the upstream disturbances and their acoustic signature at the far field. The hybrid model as well as the thermodynamic states of the engine flow-path are illustrated in Figure 1.

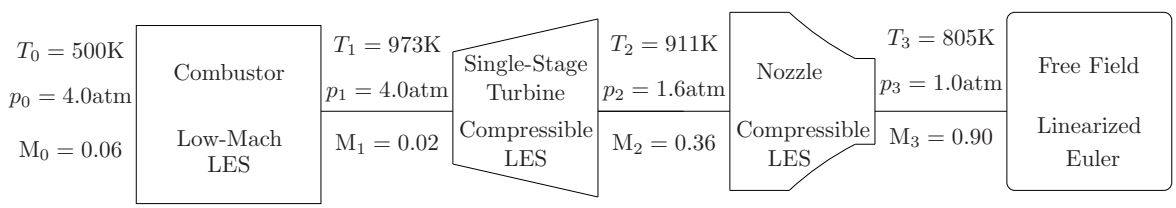

Figure 1. Summary of the component models and thermodynamic states for the flow-path of the representative gas-turbine engine.

II. Physical and numerical models

II.A. Combustor simulation

The combustor stage is modeled using the in-house code Vida, an LES solver that has previously been validated in similar applications.[7] Vida is a tool that solves the low-Mach-number formulation of the variable-density Navier–Stokes equations on unstructured grids. The code is fully implicit and second-order accurate in time and space on arbitrary grids. The chemical source term is modeled by the flamelet progress variable approach using a three-dimensional chemistry table based on tabulated chemistry for methane–air diffusion flames. The filtered momentum equation is closed using the Vreman model, and the turbulent scalar fluxes are closed using a constant turbulent Schmidt number assumption. The resulting set of governing equations is

$$\frac{\partial \bar{\rho}}{\partial t} + \frac{\partial \bar{\rho}\widetilde{u}_j}{\partial x_j} = 0 \tag{1a}$$

$$\frac{\partial \bar{\rho}\widetilde{u}_i}{\partial t} + \frac{\partial \bar{\rho}\widetilde{u}_i\widetilde{u}_j}{\partial x_j} = -\frac{\partial \bar{p}}{\partial x_i} + \frac{\partial}{\partial x_j}\left[(\bar{\mu}+\mu_t)\left(\frac{\partial \widetilde{u}_i}{\partial x_j} + \frac{\partial \widetilde{u}_j}{\partial x_i} - \frac{2}{3}\delta_{ij}\frac{\partial \widetilde{u}_k}{\partial x_k}\right)\right] \tag{1b}$$

$$\frac{\partial \bar{\rho}\widetilde{Z}}{\partial t} + \frac{\partial \bar{\rho}\widetilde{u}_j\widetilde{Z}}{\partial x_j} = \frac{\partial}{\partial x_j}\left[\left(\bar{\rho}\widetilde{D} + \frac{\mu_t}{\mathrm{Sc}_t}\right)\frac{\partial \widetilde{Z}}{\partial x_j}\right] \tag{1c}$$

$$\frac{\partial \bar{\rho}\widetilde{C}}{\partial t} + \frac{\partial \bar{\rho}\widetilde{u}_j\widetilde{C}}{\partial x_j} = \frac{\partial}{\partial x_j}\left[\left(\bar{\rho}\widetilde{D} + \frac{\mu_t}{\mathrm{Sc}_t}\right)\frac{\partial \widetilde{C}}{\partial x_j}\right] + \bar{\dot{\omega}}_c\left(\widetilde{Z}, \widetilde{Z''^2}, \widetilde{C}\right) \tag{1d}$$

$$\frac{\partial \bar{\rho}\widetilde{Z''^2}}{\partial t} + \frac{\partial}{\partial x_j}\left(\bar{\rho}\widetilde{u}_j\widetilde{Z''^2}\right) = \frac{\partial}{\partial x_j}\left[\left(\bar{\rho}\widetilde{D} + \frac{\mu_t}{\mathrm{Sc}_t}\right)\frac{\partial \widetilde{Z''^2}}{\partial x_j}\right] - \left(2\bar{\rho}\widetilde{D}\frac{\partial \widetilde{Z}}{\partial x_j}\frac{\partial \widetilde{Z}}{\partial x_j} + \bar{\rho}C\widetilde{Z''^2}\frac{\mu_t}{\mathrm{Sc}_t\Delta^2}\right). \tag{1e}$$

II.B. Turbine simulation

The turbine stage is simulated using the in-house code Charles, a fully compressible, LES solver which has been extended to incorporate moving-mesh capabilities. Structured, body-fitted grids are generated to provide an initial, coarse description of the geometry which is then refined using the in-house mesh adaptivity tool Adapt to produce an unstructured mesh with suitable resolution throughout the domain. The code is explicit and second-order accurate in time and space on unstructured grids. Charles has been validated in a variety of acoustic applications and found to perform satisfactorily.[8] The inflow conditions are constructed by averaging the combustor simulation's outflow data to obtain the impinging characteristics, and the mean pressure is imposed from the interior of the turbine computational domain. Navier-Stokes based characteristic outflow conditions are used for the outflow condition.[9] The Vreman model is used for the turbulent closure.[10] The treatment of the rotor–stator involves the construction of separate but adjacent meshes for each component and the outflow of the upstream stage is mapped onto the inflow of the downstream stage to reflect the relative motion of the blades. A second-order interpolation scheme is used for mapping values from one side of the rotor-stator interface to the other, although the fluxes at this interface are upwinded and locally first order to insure stability. Periodicity is employed to reduce computational costs; a small number of blades from each section (two from the stator and three from the rotor) are simulated with periodic boundary conditions representing effects of the full cascade. Both the rotor and the stator are modeled as being infinitely long (zero radius of curvature), so the relative motion of the blades is linear translation.

II.C. Nozzle-flow simulation

The linearized Euler equations are used to predict the interaction of the upstream disturbances with the nozzle base flow and acoustic radiation to the far field. The compressible Euler equations for entropy, velocity, and pressure are non-dimensionalized using ambient quantities. The flow variables are decomposed into a time-stationary base state (denoted by an overbar) and fluctuations around the base state (denoted by a prime) as

$$q = \bar{q} + q'. \tag{2}$$

Substituting the decomposed variables and collecting the first-order terms of the fluctuating quantities, the linearized Euler equations are obtained as

$$\frac{\partial s'}{\partial t} + \bar{\boldsymbol{u}}\cdot\boldsymbol{\nabla}s' + \boldsymbol{u}'\cdot\boldsymbol{\nabla}\bar{s} = f_s, \tag{3a}$$

$$\frac{\partial \boldsymbol{u}'}{\partial t} + \bar{\boldsymbol{u}}\cdot\boldsymbol{\nabla}\boldsymbol{u}' + \boldsymbol{u}'\cdot\boldsymbol{\nabla}\bar{\boldsymbol{u}} + \left(\frac{1}{\gamma}\frac{p'}{\bar{p}} - s'\right)\bar{\boldsymbol{u}}\cdot\boldsymbol{\nabla}\bar{\boldsymbol{u}} + \frac{1}{\bar{\rho}}\boldsymbol{\nabla}p' = f_{\boldsymbol{u}}, \tag{3b}$$

$$\frac{\partial p'}{\partial t} + \bar{\boldsymbol{u}}\cdot\boldsymbol{\nabla}p' + \boldsymbol{u}'\cdot\boldsymbol{\nabla}\bar{p} + \gamma\left(\bar{p}\boldsymbol{\nabla}\cdot\boldsymbol{u}' + p'\boldsymbol{\nabla}\cdot\bar{\boldsymbol{u}}\right) = f_p, \tag{3c}$$

where s', $\boldsymbol{u}'$, and p' are entropy, velocity, and pressure fluctuations, respectively. The base state variables are prescribed and $\gamma = c_p/c_v = 1.4$ where c_p and c_v are the specific heats at constant pressure and volume, respectively. The right-hand-side term $\boldsymbol{f} = (f_s, f_{\boldsymbol{u}}, f_p)^{\mathrm{T}}$ represents a general external forcing. The linearized equation of state is written as

$$\frac{T'}{\bar{T}} = \frac{p'}{\bar{p}} - \frac{\rho'}{\bar{\rho}}, \tag{4}$$

where the density fluctuation is computed by

$$\frac{\rho'}{\bar{\rho}} = \frac{1}{\gamma}\frac{p'}{\bar{p}} - s'. \tag{5}$$

The governing equations are directly solved for $\boldsymbol{q}' = \{s', \boldsymbol{u}', p'\}^{\mathrm{T}}$. The base state $\bar{\boldsymbol{q}}$ is obtained from a steady RANS simulation. The converged RANS solution is linearly interpolated to the grid for the linearized Euler simulation.

Spatial derivatives in the governing equations are transformed to curvilinear coordinates $\boldsymbol{\xi} = (\xi, \eta, \zeta)^{\mathrm{T}}$ using a non-singular mapping $\boldsymbol{x} = X(\boldsymbol{\xi}, \tau)$ with the inverse $\boldsymbol{\xi} = \Xi(\boldsymbol{x}, t)$. The transformation Jacobian, $J = \det(\partial \xi_i / \partial x_j)$ is positive definite. In this study, the mapping is time invariant and $\tau = t$.

The spatial discretization uses an eleven-point, explicit, wavenumber-optimized finite difference scheme.[11,12] The solution is time-advanced using the standard fourth-order Runge–Kutta method with a constant time-step size. For numerical stability, an eleven-point, explicit, optimized filter[11] is applied at every time step in every direction. The filter strength is $\sigma_d = 0.2$. To reduce the impact of the filter, filtered variables are averaged with unfiltered variables as

$$\alpha \widetilde{q} + (1 - \alpha) q, \tag{6}$$

where $0 \leq \alpha \leq 1$.

The computational domain for the linearized Euler simulations consists of multiple, overlapping blocks to represent mildly complex geometries such as a converging nozzle. In the present work, an overset-grid technique is applied to interpolate solution variables between two overlapping blocks. The fourth-order accurate interpolation stencils are generated at the pre-processing stage using Overture.[13]

Boundaries which are not updated by the overset-grid interpolation are subject to physical boundary conditions. At the inflow, solution variables obtained from the upstream SUMB simulation are prescribed in space and in time. The characteristic, non-reflecting boundary conditions are applied at the outflow and at the far field.[14,15] At solid walls, the no-penetration condition ($\boldsymbol{u} \cdot \hat{\boldsymbol{n}} = 0$) is applied, which is, in the inviscid limit, equivalent to the wall-normal pressure gradient being zero. To model the free-field radiation, an absorbing buffer zone is used.[16,17] The damping term has a quadratic distribution within the buffer zone.

III. Combustor and turbine simulation results

Preliminary results for the upstream combustor and turbine-stage simulations are shown. The combustor geometry considered is the dual-swirl gas-turbine combustor.[18] Previous work has demonstrated the current code's capability to predict the turbulent reacting flow within the same combustor.[7] To accommodate the full flow-path, the combustor simulation is run at a higher mass-flow rate and a leaner condition than has been studied experimentally. The mass-flow rate of air is 0.43 kg/s and the global equivalence ratio for methane combustion is 0.18. Air enters the combustor at 500 K and exits at 973 K. In experimental work, the combustor has demonstrated two distinct behaviors: a flat-flame mode in which the flame remains attached to the wall and a V-flame where it is unattached. At this condition, the flat flame is observed, resulting in compact combustion and increased residence time for the burnt gases to mix before passing into the turbine. The instantaneous temperature field for the combustor simulation is illustrated in Figure 2, showing the presence of the flat-flame structure.

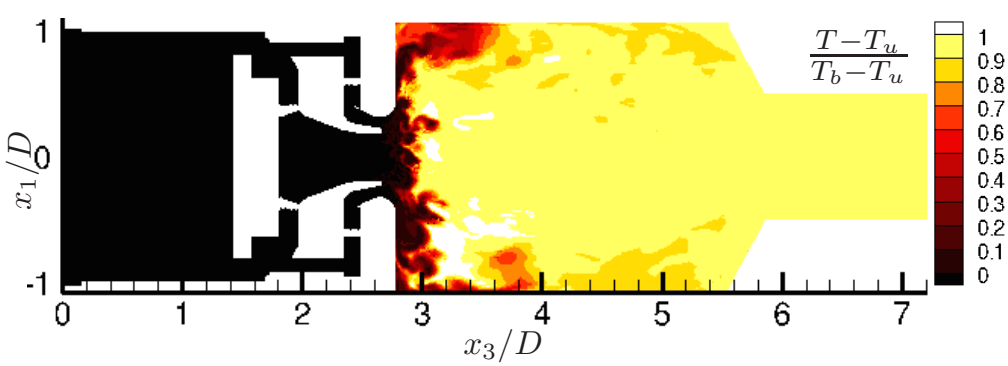

Figure 2. Instantaneous temperature contour in the gas-turbine combustor.

The turbine design considered in this study consists of a single rotor–stator pair taken from the NASA high-pressure turbine design.[19] The pressure drop over the stage is 2.37 and the large jump is used to mimic the thermodynamic effects of a multi-stage turbine. A preliminary velocity field from the turbine stage calculation is shown in Figure 3.

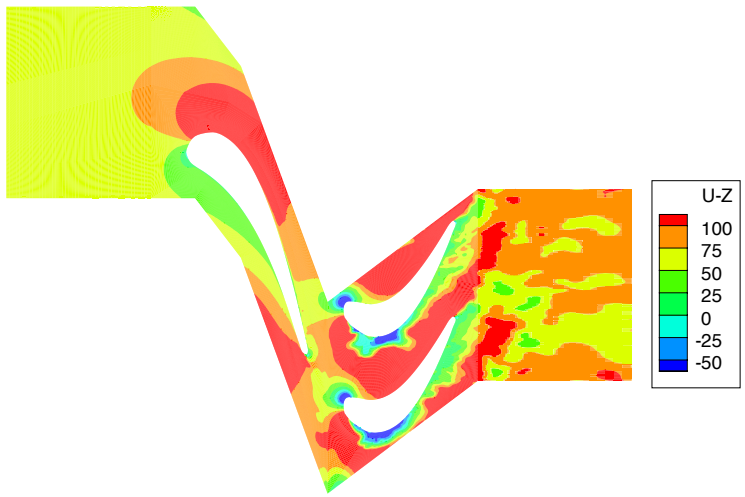

Figure 3. Instantaneous streamwise velocity contours for turbine stage simulation (in m/s).

IV. Nozzle-flow simulation results

The response of the nozzle base flow to external excitations is examined by solving the linearized Euler equations. Linear models can provide sufficiently accurate descriptions for some of the statistical features of large-scale structures within high-speed turbulent jets,[20] which are important noise sources. However, the radiated sound is predicted several orders of magnitude lower than the measurements, which implies the significance of nonlinear mechanisms in sound generation.[21] It is noted that a recent work incorporating high-fidelity LES and linear models demonstrated that the underprediction can be improved by as much as 20 dB by adopting time-dependent base flows.[22] The external excitation is prescribed as a time-harmonic plane wave at a fixed frequency, representative of fluctuations from the engine core. In this study, the linearized Euler simulation is not coupled to the upstream turbine-stage. The results provided here are intended to demonstrate the feasibility of the current linearized Euler model.

IV.A. Verification study for the linearized Euler simulation

The computational results verifying the relevant features of the linearized Euler solver for the nozzle-flow simulation are briefly discussed. Two benchmark problems from the Fourth Computational Aeroacoustics Workshop on Benchmark Problems[23] are solved using the linearized Euler solver. Detailed results on the verification studies are found elsewhere.[24]

The first problem is to predict the sound radiation of a two-dimensional parallel jet flow with an acoustic source in it. The same flow was studied by Agarwal *et al.*[25] using both analytic and numerical approaches. Radiated sound from the acoustic source propagates and is refracted by the base flow. Also, the base flow supports the spatial growth of instability waves, which overwhelm the near-field pressure signature, especially at the aft angles. The objective of this verification study is to assess if the current model accurately predicts both the direct radiation from the source and hydrodynamic fluctuations due to the amplified instability waves. Figure 4 shows instantaneous pressure fluctuations at the end of the twentieth oscillation period, corresponding to $tc_\infty/b = 441.6$, where c_∞ is the ambient speed of sound and b is the half width of the base jet. The entire simulation domain is shown and the source is located at the origin. Figure 5 compares the streamwise distribution of p' at $y = 15$ m, matching well with the previous numerical result and the corresponding analytic solution.

For the second verification study, the acoustic scattering by two rigid cylinders is computed. Scattered waves typically have amplitudes several orders-of-magnitude smaller than those of the original waves. Thus, this test is useful to assess the impact of the numerical dispersion and dissipation of the computational model. Also, the solid-wall boundary condition and the overset-grid capability are verified. Figure 6 illustrates the geometric details and overlapping grid configuration. The left cylinder has a diameter $D_{\max} = 1.0$ and the right cylinder is 50% smaller. The centerline distribution of pressure fluctuations is shown in Figure 7. The

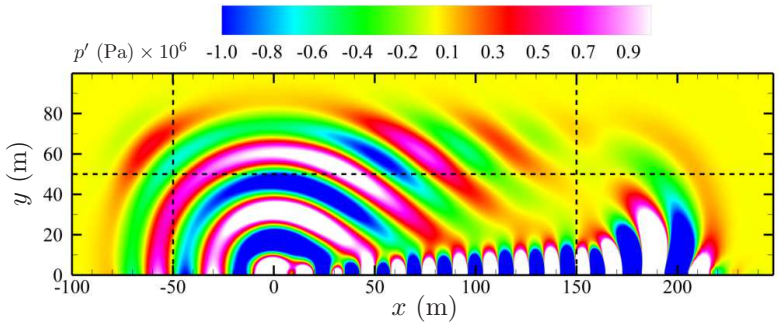

Figure 4. Pressure fluctuation contours at the end of the twentieth oscillation period ($tc_\infty/b = 441.6$). The dashed lines represent the beginning of the buffer zone.

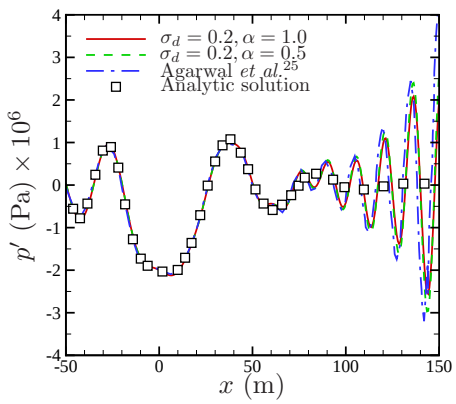

Figure 5. Instantaneous pressure fluctuations along $y = 15$ m at the end of the twentieth oscillation period ($tc_\infty/b = 441.6$). The analytic solution is found in Agarwal *et al.*[25]

quantitative agreement is good and both amplitude and phase of the scattered sound field are well predicted.

IV.B. Response of the subsonic heated jet to time-harmonic excitations

IV.B.1. Computational conditions

An axisymmetric, subsonic heated jet from a converging nozzle is simulated using the hybrid RANS and linearized Euler model to study its response to external time-harmonic excitations at a fixed frequency. In this study, the jet simulation is not coupled with the upstream turbine-stage for verification purposes. The steady RANS simulation predicts the base state of the jet flow and the linearized Euler solver computes the propagation of the hydrodynamic fluctuations and acoustic waves. Note that axisymmetry is explicitly imposed on the governing equations. The axisymmetric ($n = 0$) fluctuations are acoustically more efficient than higher-order azimuthal components,[27] especially at lower frequencies and at shallow radiation angles, which are of interest in this study regarding core-noise radiation. The external excitations are prescribed at the nozzle inlet as a boundary condition and a buffer zone with a time-harmonic target state.

A schematic of the simulation domain is shown in Figure 8(a). The same domain is used for both the RANS and linearized Euler simulations. The nozzle radius is denoted by $r_J = D_J/2 = 2.54$ cm and used as a reference length. The sharp trailing edge of the nozzle lip is rounded to avoid numerical instability. The physical domain extends $80r_J$ downstream of the nozzle exit and $80r_J$ in the radial direction. Absorbing buffer zones surround the physical domain with lengths of $10r_J$ upstream of the nozzle exit, $20r_J$ downstream

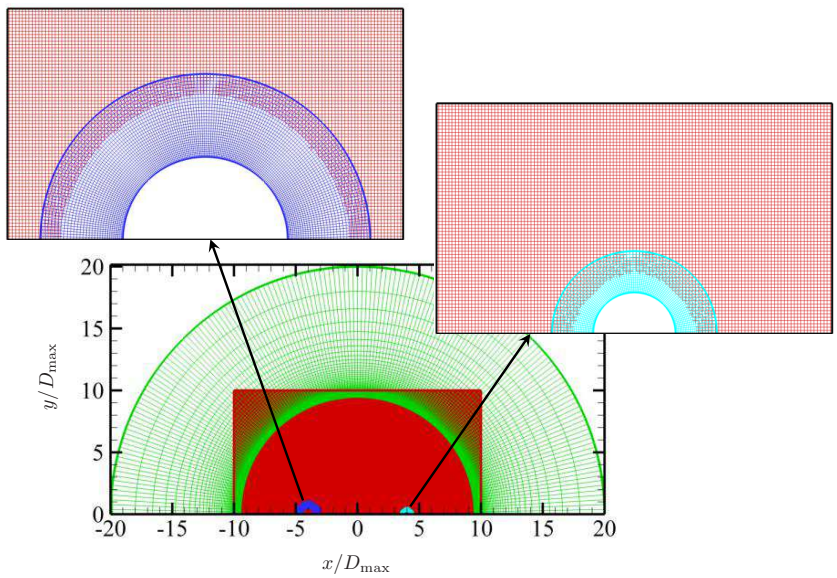

Figure 6. Computational domain and overlapping grids for cylinder scattering problem.

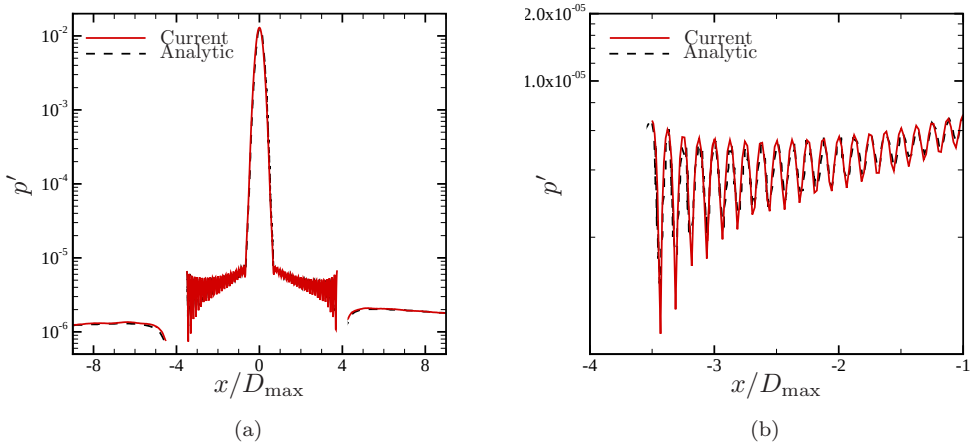

Figure 7. Root-mean-square pressure fluctuations along the centerline at $y = 0$ for (a) $-9 \leq x \leq 9$ (the physical domain) and (b) $-3.5 \leq x \leq 1$ (close to the larger cylinder). The analytic solution is taken from Sherer.[26]

of the physical outflow, and $20r_J$ in the radial direction. The center of the nozzle exit is $(x, r) = (0, 0)$, which is also the reference point to define the distance d and the radiation angle φ, where $\varphi = 0°$ corresponds to the downstream jet axis.

For the linearized Euler simulation, the converging nozzle is represented using overlapping, body-fitted grids, as illustrated in Figure 8(b). Six overlapping blocks are used for the domain and a total of 1.36×10^6 grid points are used. The grid is generated so that acoustic wave propagation up to $St_D = fD_J/U_J = 2.0$ is accurately resolved for the current finite difference scheme. The accuracy limit of 4.65 points per wavelength is used.[11] The time-step size is fixed as $\Delta t c_\infty / r_J = 5 \times 10^{-5}$.

The nozzle-exit condition matches the test-point number 49 of Tanna.[28] This is also the same as the outflow condition of the turbine stage, as illustrated in Figure 1. The non-dimensional velocity at the nozzle exit is $u_J/c_\infty = 1.48$ and the nozzle-exit temperature relative to the ambient temperature is $T_J/T_\infty = 2.857$. The jet Mach number is $M_J = u_J/c_J = 0.876$ and the Reynolds number based on the nozzle-exit condition is $Re_J = \rho_J u_J D_J/\mu_J = 2.3\times10^5$. Under the similar condition, Bertolotti & Colonius[29] studied sound generated by upstream inhomogeneities within the potential core of a subsonic hot jet using the parabolized stability

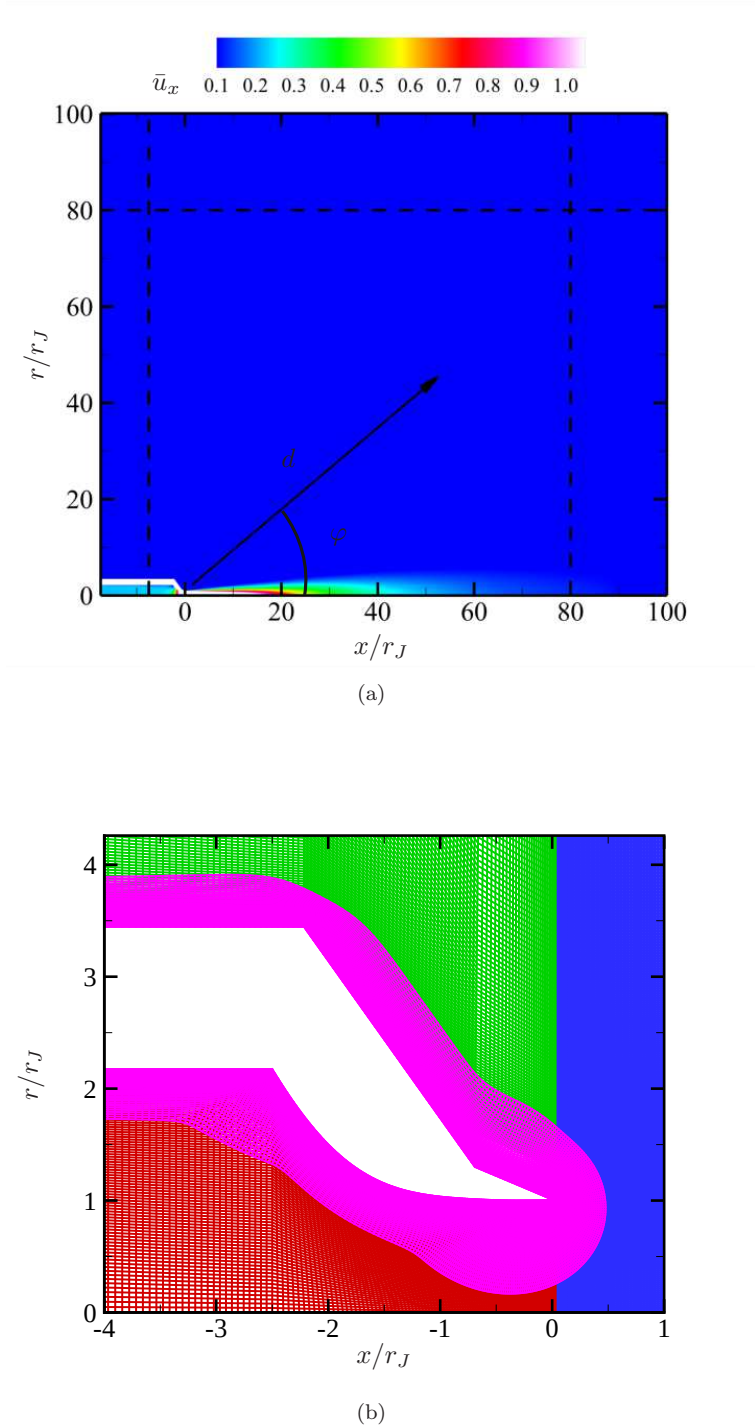

Figure 8. (a) Computational domain. The dashed lines represent the start of the buffer zone. (b) Overset-grid configuration near the nozzle exit.

equation. The jet supports a core mode efficiently coupled with the far field, and entropy fluctuations are shown to radiate more strongly than vorticity fluctuations at a realistic aircraft take-off or landing condition.

IV.B.2. Base flow simulation

Figures 9(a) and (b) show the streamwise variations of the mean axial velocity at the jet centerline and the nozzle lipline, respectively. The agreement with the particle image velocimetry (PIV) measurement of

Bridges & Wernet[30] is acceptable. The length of the potential core, defined by an axial location where $\bar{u}_x/u_J = 0.95$, is $6D_J$. The radial profiles shown in Figure 10 also agree well with the measurements. Also shown are the RANS solutions linearly interpolated onto the grid for the linearized Euler simulation. The interpolated solution is filtered by the standard eighth-order filter to selectively remove numerical noise caused by the interpolation. The boundary-layer thickness of the separating boundary layer slightly upstream of the nozzle exit is $\delta_{99}/r_J = 0.065$ and resolved by 21 points for the linearized Euler simulation. The momentum thickness is $\delta_m/r_J = 0.045$ where 17 points are used. The rounding radius of the nozzle trailing edge is 3% of δ_m. This appears to be rather small and the nozzle trailing edge is deemed sharp compared with the incoming boundary layer. However, the selective filtering suppresses numerical instability. The comparison demonstrates that the current RANS prediction is sufficiently accurate to describe the time-averaged state of the corresponding turbulent jet.

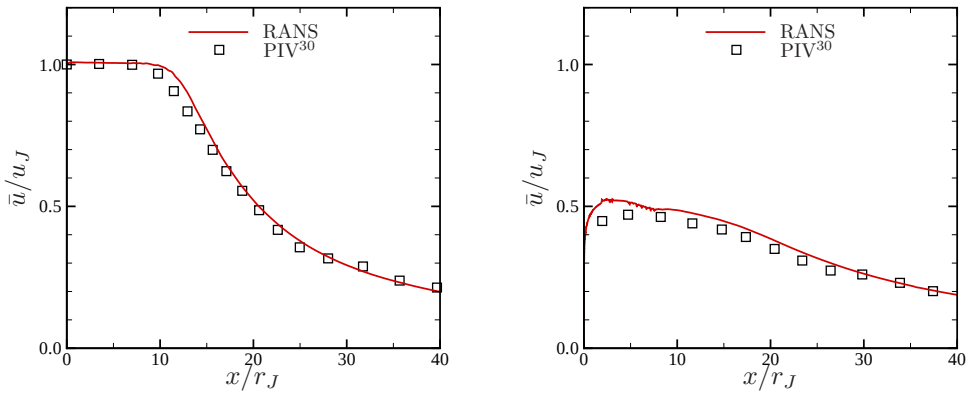

Figure 9. Spatial profiles of mean axial velocity along (a) the centerline ($r = 0$) and (b) the nozzle lipline ($r/r_J = 1$).

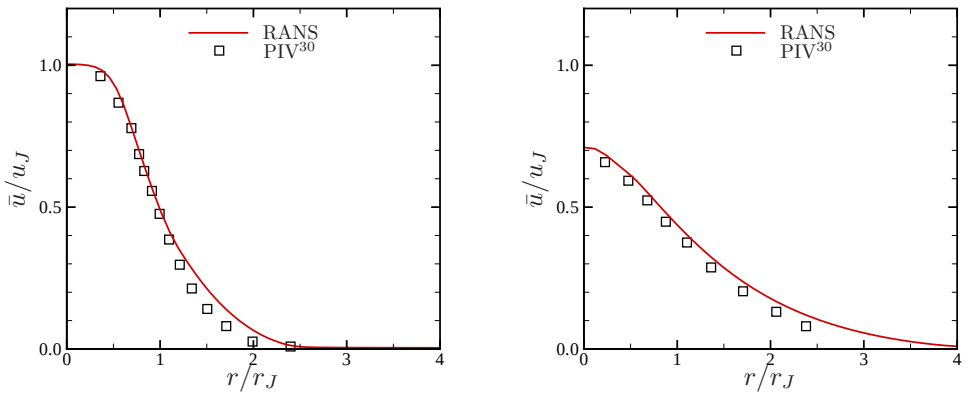

Figure 10. Radial profiles of mean axial velocity (a) at $x/D_J = 4$ and (b) at $x/D_J = 8$.

IV.B.3. Propagation of the incident plane acoustic waves in the ambient base state

Before studying the interactions between the base jet flow and the incident entropy fluctuations, propagation of the incident plane acoustic waves through the converging nozzle into a homogeneous and isentropic medium is simulated. This test assesses the impact of the converging nozzle on the wave propagation at several frequencies. Also, the resolution properties of the computational grid, overset-grid interpolation, and discretization are assessed.

The base state is ambient and isentropic. At the nozzle inlet, time-harmonic plane acoustic waves are prescribed. The incident waves propagate in the axial direction within the nozzle and then radiate to the far field. The maximum amplitude is 0.5% of the ambient pressure p_∞ and corresponds to 150dB for the reference pressure $p_{\text{ref}} = 20\ \mu$Pa. Six excitation frequencies are considered: $St_D = 0.02$, 0.04, 0.4, 0.74, 1.0, and 2.0. The first two are chosen close to the frequencies of the fluctuations generated in the engine core.[1,2] The frequency $St_D = 0.4$ corresponds to the jet preferred mode frequency, and $St_D = 0.74$ is approximately a harmonic of the preferred frequency with its wavelength slightly shorter than the nozzle-exit diameter, which is the theoretical frequency at which acoustic diffraction becomes important. Parameters for the incident plane waves are summarized in Table 1. In this section, only the results for $St_D = 0.04, 0.4, 0.74$, and 2.0 are presented. The incident acoustic waves at different frequencies have the same fluctuation energy when averaged over a single oscillation period.

Table 1. Parameters for the incident time-harmonic plane waves.

St_D	f(Hz)	λ/r_J
0.02	200	70
0.04	400	35
0.4	4×10^3	3.5
0.74	7.3×10^3	1.9
1.0	10×10^3	1.4
2.0	20×10^3	0.7

Figures 11(a) through (d) show the propagation of the incident plane acoustic waves at several frequencies. Overall, wave fronts are well represented over nearly two decades of frequencies. At lower frequencies (thus, longer waves), the incident acoustic waves are simply transmitted to the far field. Due to the relatively rapid contraction of the nozzle area, upstream reflections are observed for $St_D > 0.4$. The propagation of higher-frequency waves (thus, shorter wavelengths) is mildly affected by the overset-grid interpolation and different grid resolution between two adjacent blocks, which is visible along $r/r_J = 18$ in Figure 11(d). For the highest frequency considered in this study ($St_D = 2.0$ and $\lambda/D_J = 0.35$), strong acoustic diffraction is observed, as demonstrated in Figure 11(d). The angle at which the diffracted acoustic intensity takes its first minimum can be estimated by $\varphi_{\min} = \sin^{-1}(\lambda/D_J)$ using a geometric argument in the far-field limit,[31] which matches with the numerical results in Figure 11(d). In Figure 12, normalized acoustic intensity at $d/r_J = 20$ compares well with the analytic Airy diffraction pattern for a circular aperture.[31]

Figure 13(a) shows the decay of sound pressure level (SPL) along a line of $\varphi = 30°$. For $d/r_J \gtrsim 20$, SPL decays at a correct rate d^{-4} (with some frequency and angle dependence) and near-field scattered sounds become less significant. The strong diffraction at $St_D = 2.0$ causes a substantial reduction in SPL (≈ 40 dB) compared to the lower frequency wave propagation. Sound directivity is shown in Figure 13(b) at $d/r_J = 20$. At lower frequencies, SPL is relatively uniform over φ (within 3 to 6 dB) and simple transmission is dominant. As frequency increases and acoustic diffraction becomes important ($St_D \gtrsim 0.74$), sound radiation depends strongly on φ.

IV.B.4. Perturbed base jet and its acoustic radiation: incident plane acoustic waves

In realistic gas-turbine engines, fluctuations entering the exhaust nozzle consist of entropic, vortical, and acoustic fluctuations and their complicated interactions. Acoustic waves can efficiently amplify instability waves in the jet shear layer and thus, can significantly change sound radiation.[32] Also, some of the incident acoustic fluctuations directly transmit (refracted by the mean flow) to the far field, which should be distinguished from sound generated by instability waves and indirect core noise to evaluate the relative importance of the noise sources.

In this section, the base jet flow is perturbed by time-harmonic plane acoustic waves and its response is examined for a range of frequencies. The maximum amplitude and frequencies are kept the same as the previous cases for the ambient base state. The result for $St_D = 2.0$ is not included since the base jet does not respond to excitations at this frequency.

Figures 14(a) through (d) show the instantaneous pressure contours for several excitation frequencies. It is well known that round jets are most responsive to disturbances at $0.2 \leq St_D \leq 0.4$, generating large-

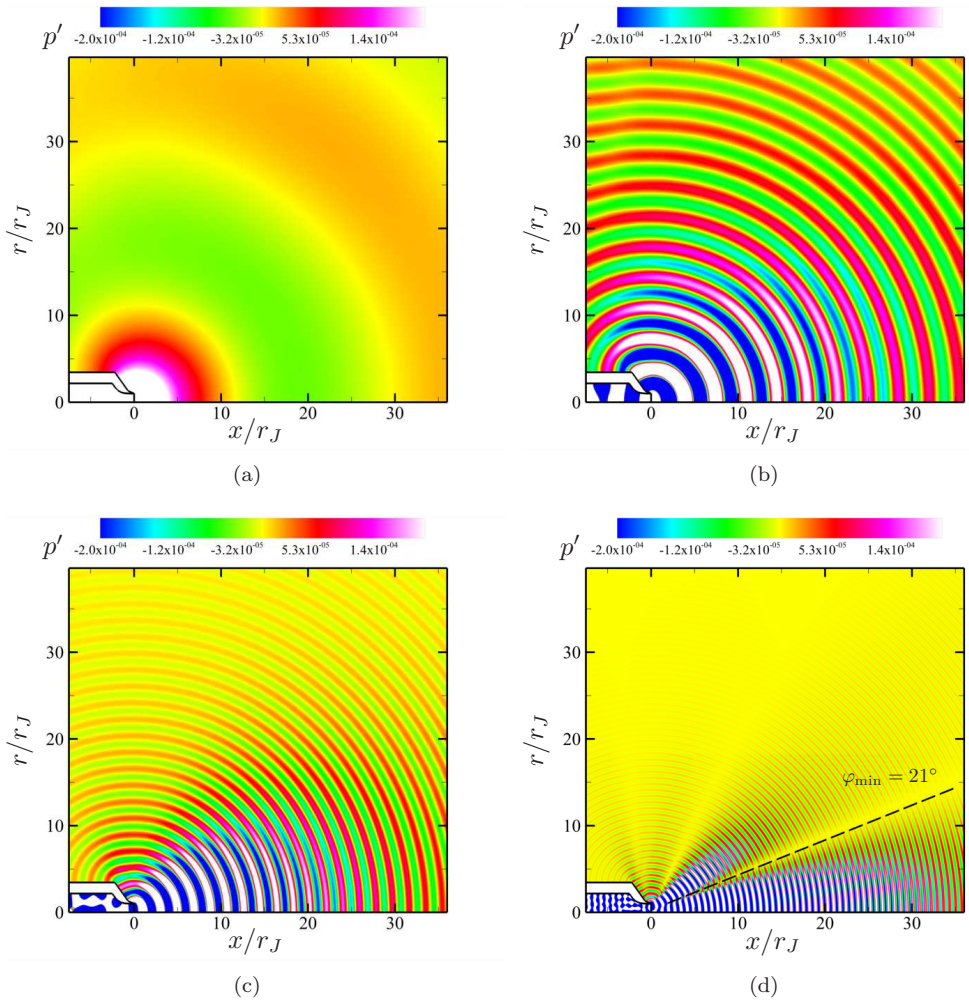

Figure 11. Instantaneous pressure fluctuations at $tc_\infty/r_J = 93.5$ for (a) $St_D = 0.04$; (b) $St_D = 0.4$; (c) $St_D = 0.74$; (d) $St_D = 2.0$.

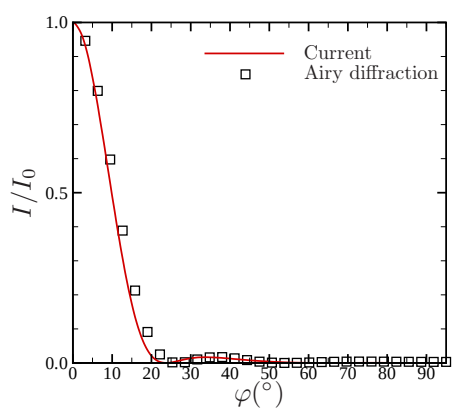

Figure 12. Normalized acoustic intensity on an arc of $d/r_J = 20$. The reference acoustic intensity I_0 is given by $I(\varphi = 0°)$.

scale, organized vortical structures known as the jet preferred mode.[32] Figure 14(b) shows qualitatively similar amplification of large-scale structures and their eventual decay as they convect downstream. In subsonic jets, the growth–saturation–decay cycle of the convecting wavepackets[20] renders some fluctuations radiation-capable, and strongly directed radiation is observed at the forward angles, which can be seen

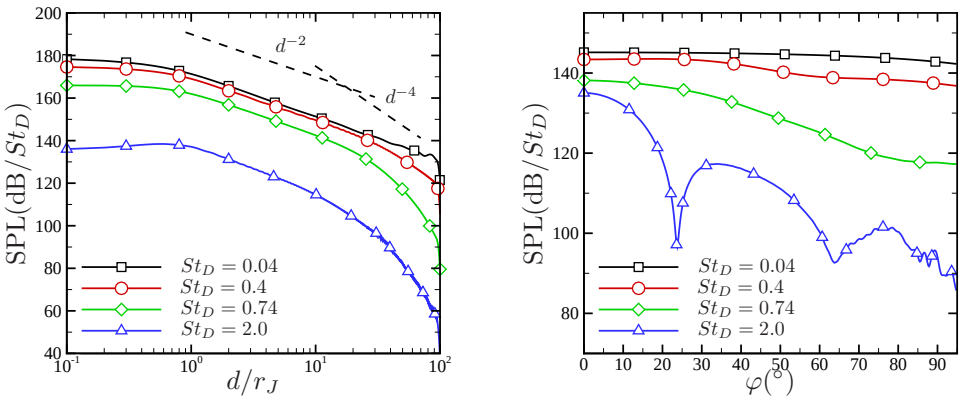

(a) (b)

Figure 13. (a) The decay of SPL along a line of $\varphi = 30^\circ$ and (b) the directivity at $d/r_J = 20$.

between $\varphi = 15^\circ$ and 40° in Figure 14(b). The angle at which sound radiation is maximum is $\varphi_{\max} = 25^\circ$. The base jet shows a similar but weaker near-field response for $St_D = 0.74$. However, the jet is not strongly coupled with the acoustic far field, which is also the case for $St_D = 1.0$ shown in Figure 14(d).

In Figure 15, the sound radiation of the jet excited at $St_D = 0.4$ is compared with the superdirectivity model.[33–35] In high-speed jet flows, sound radiation at lower angles often demonstrates an exponential decay in φ, $p' \sim \exp[-(kL)^2(1 - M_c \cos\varphi)^2/4]$, where L is a characteristic length scale and M_c is the convective Mach number. This exponential variation is one of the physically significant aspects of subsonic jet noise and is well-predicted by the current simulation.

The response of the base jet at $St_D = 0.04$ is more relevant to core-noise propagation since fluctuations generated within engine cores are characterized by the frequencies of several hundred Hz.[1] In Figure 14(a), the pressure response shows the existence of modulated wavepackets and transmitted sound at the excitation frequency. As shown in Figure 16(a), the wavepacket convects at $u_c/u_J \approx 0.38$ and slows down at $x/r_J \approx 30$ to $u_c/u_J \approx 0.18$. The wavepacket grows in amplitude, saturates at $x/r_J \approx 20$, and slowly decays, as illustrated in Figure 17(a). It is correlated over $50r_J$ in the axial direction. For comparison, similar space–time contours for $St_D = 0.4$ are shown in Figure 16(b). At this excitation frequency, the conventional eddy convective velocity $u_c/u_J \approx 0.7$ is obtained and the modulated wavepacket is correlated over $20r_J$ in the axial direction, shorter than for $St_D = 0.04$.

Based upon these observations, the low-frequency wavepacket for $St_D = 0.04$ might become radiation capable even at the subsonic convection velocity $u_c/c_\infty \approx 0.56$. This is important for assessing the impact of entropy fluctuations on sound radiation, since the two mechanisms are fundamentally different. Figure 18(a) shows sound directivity at $d/r_J = 80$ for $St_D = 0.04$. Sound radiations for the ambient and base jet states are shown, respectively. Compared to the ambient base state, the base jet flow significantly amplifies sound at lower radiation angles ($\varphi \lesssim 60^\circ$). When integrated over φ, the amplification corresponds to ~ 12 dB. Along the side-line direction, SPL remains comparable. Similarly, sound directivity is shown for the jet excited at $St_D = 0.4$ in Figure 18(b). The base jet demonstrates considerable preferential radiation, as discussed regarding Figure 15, while radiation is more or less uniform in φ for the ambient base state. The integrated SPL over φ for each base state differs within 1 dB.

This result suggests that the jet excited at $St_D = 0.04$ might, to some extent, radiate sound to lower polar angles. However, the acoustic efficiency could be overestimated as the current domain supports only up to two or three wavelengths for $St_D = 0.04$ (see Figure 14(a)). Thus, it is possible that near-field effects persist at the measured location $d/r_J = 80$. Also, compared to $St_D = 0.4$ where the jet strongly radiates, SPL at shallow radiation angles is substantially amplified, again suggesting that non-propagating hydrodynamic fluctuations remain at $d/r_J = 80$, especially at lower radiation angles. This can be evidenced by the slowly decaying entropy wavepackets for $St_D = 0.04$ shown in Figure 19(a). Although the magnitudes become relatively small, their near-field signature is still visible near the outlet of the physical domain. In Figure 19(b), the entropy wavepackets at $St_D = 0.4$ decay to negligible amplitudes. Increasing the domain size both in the axial and in the radial directions to accommodate a sufficient number of wavelengths (10 to

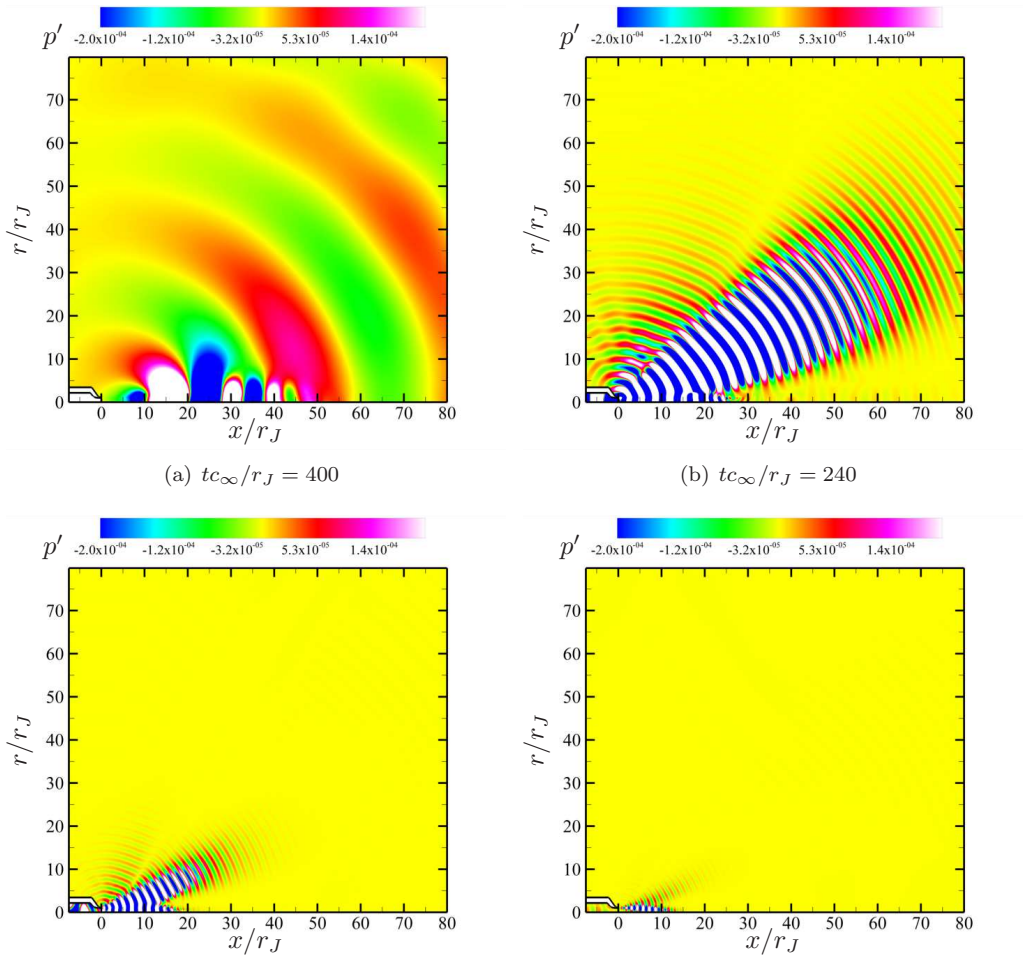

(a) $tc_\infty/r_J = 400$ (b) $tc_\infty/r_J = 240$

(c) $tc_\infty/r_J = 142$ (d) $tc_\infty/r_J = 183$

Figure 14. Instantaneous pressure fluctuations for the excitation frequency of (a) $St_D = 0.04$; (b) $St_D = 0.4$; (c) $St_D = 0.74$; (d) $St_D = 1.0$.

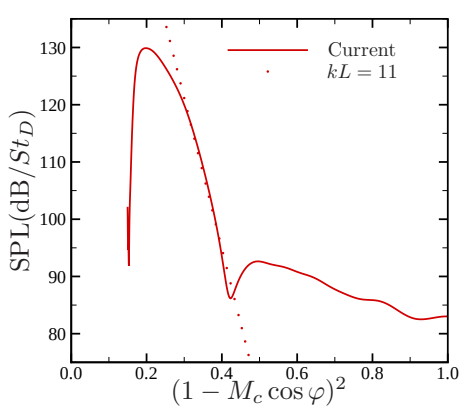

Figure 15. Sound directivity at $d/r_J = 80$ for the jet excited at $St_D = 0.4$.

20) is necessary. This effort is currently underway.

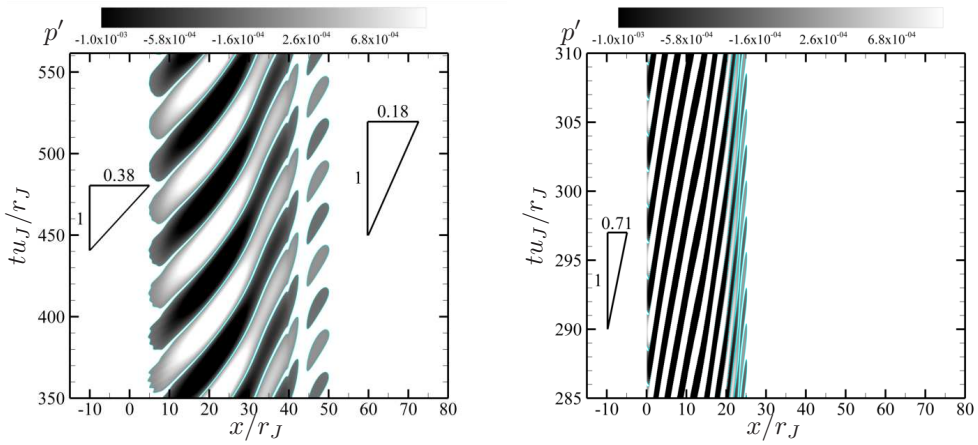

(a) (b)

Figure 16. Space–time contours of pressure fluctuations at $r/r_J = 1.5$ for the jet excited at (a) $St_D = 0.04$ and (b) $St_D = 0.4$.

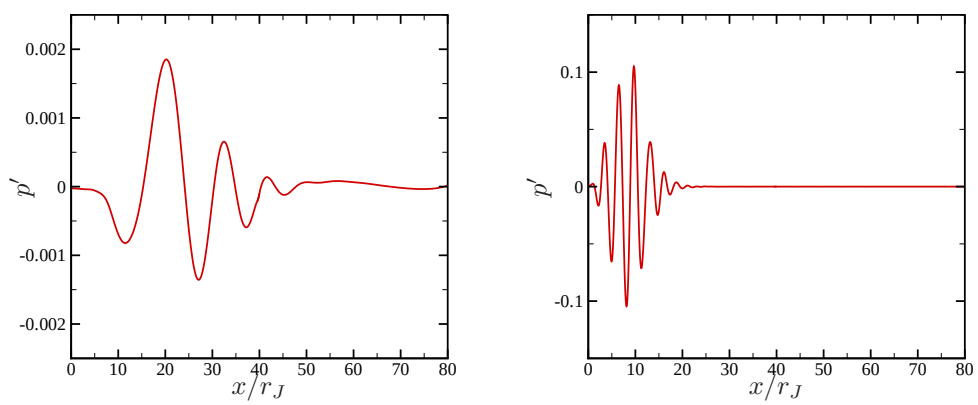

(a) (b)

Figure 17. Instantaneous pressure fluctuations at $r/r_J = 1.5$: (a) $St_D = 0.04$ and $tu_J/r_J = 500$ and (b) $St_D = 0.4$ and $tu_J/r_J = 300$.

IV.B.5. Perturbed base jet and its acoustic radiation: incident entropy fluctuations

The receptivity of the base jet to time-harmonic entropy fluctuations is discussed in this section. Thus, for the linearized Euler equations in Section II.C, only the right-hand side of the entropy equation (3a) is non-zero. Three excitation frequencies are examined based upon the results of the previous sections: $St_D = 0.04$, 0.4, and 1.0. It was found that the base jet responds only to the entropy fluctuations at $St_D = 0.04$. Thus, only the results for $St_D = 0.04$ are reported in this paper. The maximum amplitude corresponds to a 5% fluctuation in temperature ($\approx$ 50K), close to the temperature fluctuations in commercial jet-engine exhaust. The spatial distribution of the incident entropy fluctuation is varied to assess its effect on near-field and acoustic responses. Two different distributions are considered: uniform and Gaussian profiles. The Gaussian profile has a radial distribution of $\exp[-\ln(2)(r/w_{0.5})^2]$, where $w_{0.5} = 0.5r_J$. Thus, near the jet axis, entropy fluctuations are largest and they become negligible near the interior wall of the nozzle.

In Figure 20(a) and (b), the instantaneous contours of entropy fluctuations at $tc_\infty/r_J = 400$ are plotted for two different spatial profiles of entropy fluctuations, respectively. Note that the result for the base jet forced by acoustic waves at the same frequency is shown in Figure 19(a). Within the exhaust nozzle, the incident entropy fluctuations are convected at local mean velocities ($\approx 0.2u_J$) and accelerated by the mean velocity gradients at the converging section. In the potential core, the base jet is supersonic with respect to the ambient air ($u_J/c_\infty = 1.48$), which significantly stretches the entropy fluctuations in the axial direction.

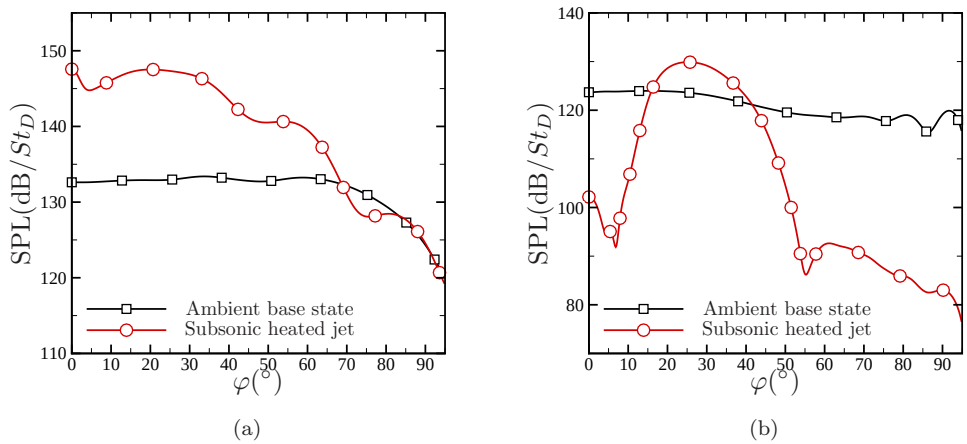

Figure 18. Comparisons of sound directivity between the ambient base state and the base jet flow at $80r_J$ for the excitation frequencies of (a) $St_D = 0.04$ and (b) $St_D = 0.4$.

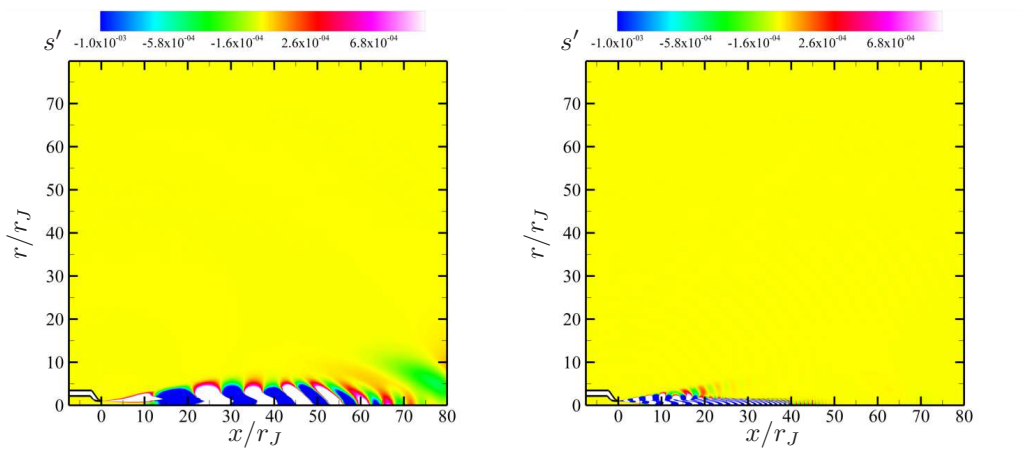

Figure 19. Instantaneous entropy fluctuations for the excitation frequency of (a) $St_D = 0.04$ and (b) $St_D = 0.4$.

For both frequencies, the low-frequency wavepackets similar to those observed in Figure 19(a) are excited, where the uniform entropy excitation is more efficient in amplifying the amplitudes for its higher level of fluctuations near the nozzle trailing edge. At $x/r_J = 80$, transient interactions between decaying entropy wavepackets and the outflow buffer zone are observed. Their amplitudes decay in time, but the rate is very slow since entropy fluctuations travel at local mean velocities. However, their impact on pressure fluctuations seems insignificant since the mean flow gradients near the domain outflow are negligible and thus, entropy is essentially decoupled from pressure.

Figure 21(a) and (b) show the instantaneous contours of pressure fluctuations at $tc_\infty/r_J = 400$. In Figure 21(a), the jet response to the uniform distribution of the entropy fluctuations is qualitatively similar to Figure 14(a), where the base jet is perturbed by acoustic waves. The qualitative similarity is presumably caused by the indirect mechanism where upstream entropy fluctuations are accelerated by mean flow gradients and some of the energy are converted into pressure fluctuations. Thus, the near-field wavepackets are excited in a similar way with that for the incident acoustic waves.

Regarding Figure 21(a), an interesting question is whether the radiated sound is primarily generated by the indirect mechanism in the converging nozzle or the low-frequency wavepackets contribute as well. This can be addressed by comparing the results for the two different distributions of incident entropy excitations. By using the Gaussian distribution, the incident entropy fluctuations near the nozzle trailing edge remain small. This results in reduced pressure fluctuations near the nozzle trailing edge (converted by the indirect

mechanism) and thus, less amplified wavepackets, which can be seen in Figure 21(b). If the indirect noise dominates over sound generated by the low-frequency wavepackets, the radiated sound in Figure 21(b) should be essentially the same compared to that in Figure 21(a).

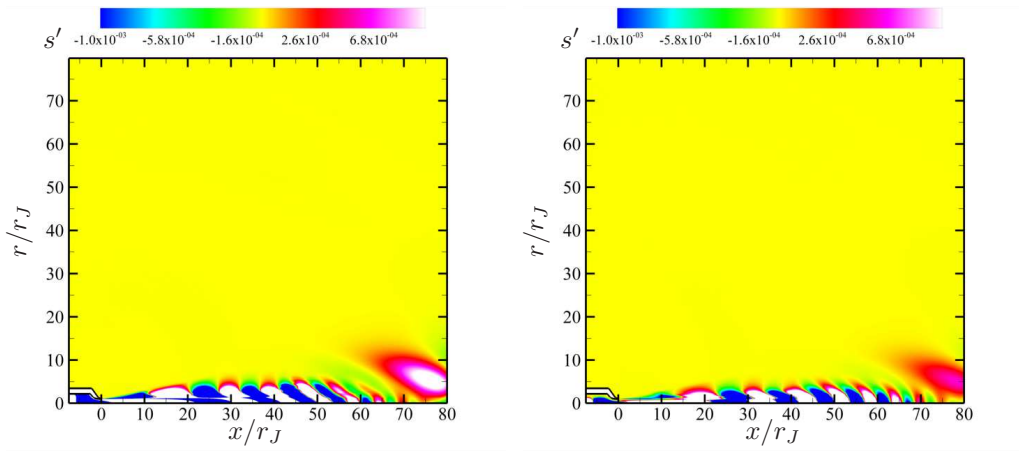

Figure 20. Instantaneous entropy fluctuations for $St_D = 0.04$ at $tc_\infty/r_J = 400$: (a) uniform spatial distribution and (b) Gaussian distribution.

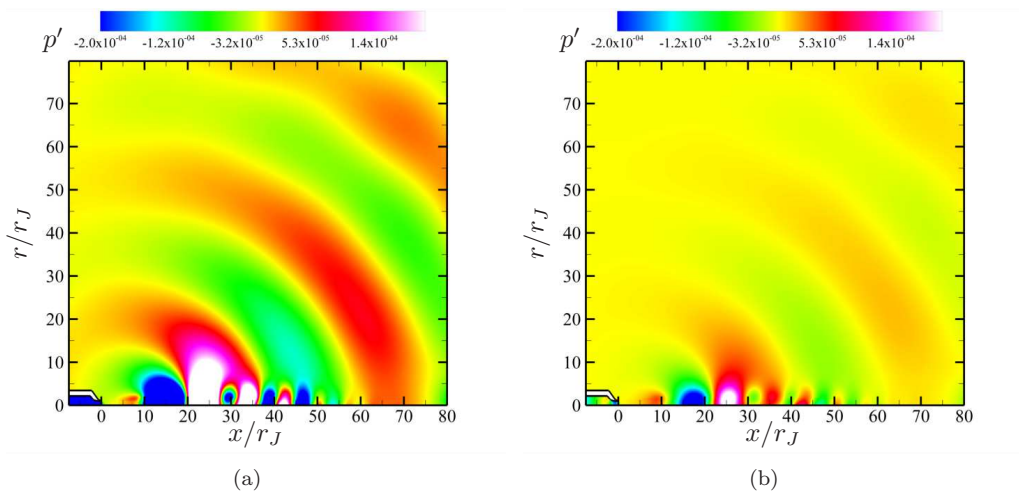

Figure 21. Instantaneous pressure fluctuations for $St_D = 0.04$ at $tc_\infty/r_J = 400$: (a) uniform spatial distribution and (b) Gaussian distribution.

In Figure 22(a), sound directivity of the base jet is shown for different types of external excitations. Compared to the acoustically-excited jet, the result for the uniform entropy fluctuations shows more radiation (2 to 4 dB) toward $\varphi \gtrsim 30°$. However, the two cases do not have exactly the same excitation energy, so this comparison should be interpreted qualitatively. For the Gaussian entropy fluctuations, SPL shows more than 10 dB reduction compared to that of the uniform fluctuations. However, since the two spatial distributions do not have same energy at the nozzle inlet (the uniform distribution has four times larger entropy fluctuations than the Gaussian distribution), SPL for the Gaussian fluctuations is shifted by 12 dB based upon the linearity of the problem. Once shifted, the two curves for the entropy fluctuations collapse. This concludes that the low-frequency wavepackets in Figure 21(a) and presumably in Figure 14(a) are not efficient noise sources and for the excitations at $St_D = 0.04$, the indirect noise generated by the converging nozzle is a dominant radiated sound.

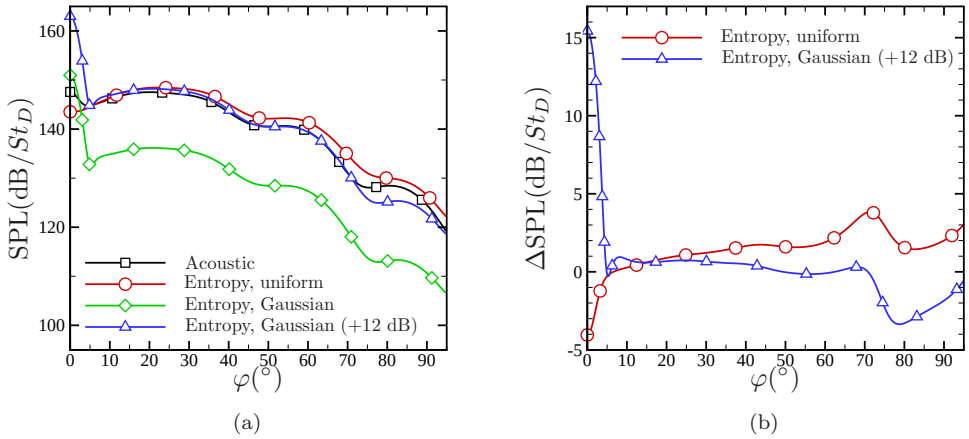

Figure 22. (a) Sound directivity of the base jet excited at $St_D = 0.04$ for different types of forcings and (b) relative SPL compared to the acoustically-excited jet at $St_D = 0.04$.

V. Summary and future work

A hybrid modeling approach to predict the engine core noise from a modeled gas-turbine engine and assess its receptivity to time-harmonic excitations is proposed. The modeled core-noise system consists of combustor, single-stage turbine, converging nozzle, and free-field radiation to the acoustic far field. The computational strategy for the generation and propagation of turbulent fluctuations from the combustor to the nozzle exhaust is developed. In this paper, modeling tools for the individual components are separately developed and tested without coupling. Combustor and turbine-stage simulations are on-going and the paper focuses on the nozzle-flow simulation.

To predict the development of near-field fluctuations and acoustic radiation to the far field, a linear analysis based upon solving the linearized Euler equations by the non-dissipative high-order optimized finite difference scheme is implemented and verified. The benchmark problems are selected to verify the code's capabilities such as overset-grid interpolation and boundary conditions relevant to the core-noise prediction. The quantitative agreement with the analytic solutions is good. Also, the impact of numerical dispersion and dissipation is carefully assessed for the benchmark problems.

Hybrid RANS and linearized Euler simulations are performed to examine the base-state response of the subsonic heated jet matching the turbine-stage outflow condition. First, time-harmonic plane acoustic waves are prescribed at the nozzle inlet. Ambient, isentropic base state and RANS-predicted subsonic heated jet flow are examined. The acoustic response of the converging nozzle is assessed for various frequencies over two decades. The base jet flow demonstrates selective response to the imposed frequencies. The frequencies which can trigger the jet preferred mode support convecting wavepacket structures and strong radiation at lower emission angles, while the incident waves at $St_D = O(1)$ are not particularly amplified.

For time-harmonic entropy fluctuations, the base jet responds to only the low-frequency excitation at $St_D = 0.04$. For that frequency, the effects of the spatial distributions are examined. Within the converging nozzle, the indirect mechanism converts some of the entropy fluctuations to pressure fluctuations, some of which excite the wavepackets and radiate. It is found out that the indirect noise is a primary noise source at this frequency.

Future work will focus on directly coupling the upstream combustor and turbine simulations to provide more realistic inflow disturbances to the linearized Euler simulation. In parallel, theoretical frameworks for the noise-receptivity study will be developed using more sophisticated analysis tools based upon global stability theory or adjoint. The upstream fluctuations will be replaced by more realistic eigenfunctions obtained by, for example, the spatial stability analysis of the nozzle internal flow or the proper orthogonal decomposition of the turbine outflow data. The analysis will then examine in detail the impacts of the disturbance eigenfunctions on sound generation and radiation. Also, the effects of combining entropy, vorticity, and acoustic fluctuations will be investigated.

Acknowledgments

The authors acknowledge the following award for providing computing and visualization resources that have contributed to the research results reported within this report: MRI-R2: Acquisition of a Hybrid CPU/GPU and Visualization Cluster for Multidisciplinary Studies in Transport Physics with Uncertainty Quantification (`http://www.nsf.gov/awardsearch/showAward.do?AwardNumber=0960306`). This award is funded under the American Recovery and Reinvestment Act of 2009 (Public Law 111-5).

The authors are grateful to Prof. Juan Alonso and Dr. Edwin van der Weide for providing the SUMB code. The first author acknowledges the Stanford Graduate Fellowship program for continued support of this work. The authors are also grateful to Dr. Yee Chee See and Prof. Sanjiva Lele for useful discussions.

References

[1]Strahle, W. C., "Combustion noise," *Prog. Energy Combust. Sci.*, Vol. 4, No. 3, 1978, pp. 157–176.

[2]Hubbard, H. H., "Aeroacoustics of flight vehicles: Theory and practice. Vol. 1. Noise sources," DTIC Document, 1991.

[3]Motheau, E., Nicoud, F., and Poinsot, T., "Mixed acoustic–entropy combustion instabilities in gas turbines," *J. Fluid Mech.*, Vol. 749, 2014, pp. 542–576.

[4]Muthukrishnan, M., Strahle, W. C., and Neale, D. H., "Separation of hydrodynamic, entropy, and combustion noise in a gas turbine combustor," *AIAA J.*, Vol. 16, No. 4, 1978, pp. 320–327.

[5]Leyko, M., Nicoud, F., and Poinsot, T., "Comparison of direct and indirect combustion noise mechanisms in a model combustor," *AIAA J.*, Vol. 47, No. 11, 2009, pp. 2709–2716.

[6]See, Y. C., Amini, G., Koh, C., and Ihme, M., "Jet noise receptivity to nozzle-upstream perturbations in compressible heated jets," 18th AIAA/CEAS Aeroacoustics Conference (33rd AIAA Aeroacoustics Conference), Colorado Springs, Colorado, 2012, AIAA Paper No. 2012–2259.

[7]See, Y. C. and Ihme, M., "Large eddy simulation of a partially-premixed gas turbine model combustor," *Proc. Combust. Inst.*, Vol. 35 (in press.), 2014.

[8]Khalighi, Y., Ham, F., Moin, P., Lele, S., Colonius, T., Schlinker, R., Reba, R., and Simonich, J., "Unstructured large eddy simulatino technology for prediction and control of jet noise," .

[9]Poinsot, T. and Lele, S., "Boundary conditions for direct simulations of compressible viscous flows," *Journal fo Computational Physics*, Vol. 101, 1992, pp. 104–129.

[10]Vreman, B., Guerts, B., and Kuerten, H., "Subgrid-modelling in LES of compressible flow," *Applied Scientific Research.*

[11]Bogey, C. and Bailly, C., "A family of low dispersive and low dissipative explicit schemes for flow and noise computations," *J. Comput. Phys.*, Vol. 194, No. 1, 2004, pp. 194–214.

[12]Berland, J., Bogey, C., Marsden, O., and Bailly, C., "High-order, low dispersive and low dissipative explicit schemes for multiple-scale and boundary problems," *J. Comput. Phys.*, Vol. 224, No. 2, 2007, pp. 637–662.

[13]Brown, D. L., Henshaw, W. D., and Quinlan, D. J., "Overture: Object-oriented tools for overset grid applications," 17th Applied Aerodynamics Conference, Norfolk, Virginia, 1999, AIAA Paper No. 99–3130.

[14]Poinsot, T. J. and Lele, S. K., "Boundary conditions for direct simulations of compressible viscous flows," *J. Comput. Phys.*, Vol. 101, 1992, pp. 104–129.

[15]Kim, J. W. and Lee, D. J., "Generalized characteristic boundary conditions for computational aeroacoustics," *AIAA J.*, Vol. 38, No. 11, 2000, pp. 2040–2049.

[16]Freund, J. B., "Proposed inflow/outflow boundary condition for direct computation of aerodynamic sound," *AIAA J.*, Vol. 35, No. 4, 1997, pp. 740–742.

[17]Bodony, D. J., "Analysis of sponge zones for computational fluid mechanics," *J. Comput. Phys.*, Vol. 212, No. 2, 2006, pp. 681–702.

[18]Meier, W., Weigand, P., Duan, X. R., and Giezendanner-Thoben, R., "Detailed characterization of the dynamics of thermoacoustic pulsations in a lean premixed swirl flame," *Combust. Flame*, Vol. 150, 2007, pp. 2–26.

[19]Stabe, R. G. and Schwab, J. R., "Performance of a high-work, low-aspect-ratio, turbine stator tested with a realistic inlet radial temperature gradient," NASA/TM–1991-103738, National Aeronautics and Space Administration Lewis Research Center, Cleveland, Ohio, 1991.

[20]Jordan, P. and Colonius, T., "Wave packets and turbulent jet noise," *Annu. Rev. Fluid Mech.*, Vol. 45, No. 1, 2013, pp. 173–195.

[21]Cheung, L. C. and Lele, S. K., "Linear and nonlinear processes in two-dimensional mixing layer dynamics and sound radiation," *J. Fluid Mech.*, Vol. 625, 2009, pp. 321–351.

[22]Jordan, P., Colonius, T., Bres, G. A., Zhang, M., Towne, A., and Lele, S., "Modeling intermittent wavepackets and their radiated sound in a turbulent jet," Proceedings of the Summer Program, Center for Turbulence Research, Stanford University/NASA Ames (to appear), 2014.

[23]Dahl, M., "Fourth Computational Aeroacoustics (CAA) Workshop on Benchmark Problems," NASA CP–2004-212954, Cleveland, OH, 2004.

[24]Kim, J., O'Brien, J., and Ihme, M., "Linear analysis of engine core noise using a hybrid modeling approach," Annual Research Briefs, Center for Turbulence Research, Stanford University/NASA Ames, 2014.

[25]Agarwal, A., Morris, P. J., and Mani, R., "Calculation of sound propagation in nonuniform flows: suppression of instability waves," *AIAA J.*, Vol. 42, No. 1, 2004, pp. 80–88.

[26]Sherer, S. E., "Scattering of sound from axisymetric sources by multiple circular cylinders," *J. Acoust. Soc. Am.*, Vol. 115, No. 2, 2004, pp. 488–496.

[27]Michalke, A. and Fuchs, H. V., "On turbulence and noise of an axisymmetric shear flow," *J. Fluid Mech.*, Vol. 70, 1975, pp. 179–205.

[28]Tanna, H. K., "An experimental study of jet noise Part I: Turbulent mixing noise," *J. Sound Vib.*, Vol. 50, No. 3, 1977, pp. 405–428.

[29]Bertolotti, F. and Colonius, T., "On the noise generated by convected structures in a Mach 0.9 hot, turbulent jet," 41st Aerospace Sciences Meeting and Exhibit, Reno, Nevada, 2003, AIAA Paper No. 2003–1062.

[30]Bridges, J. and Wernet, M. P., "The NASA subsonic jet particle image velocimetry (PIV) dataset," NASA/TM–2011-216807, National Aeronautics and Space Administration Glenn Research Center, Cleveland, Ohio, 2011.

[31]Pierce, A. D., *Acoustics: An introduction to its physical principles and applications*, Acoustical Society of America, 1989.

[32]Crow, S. C. and Champagne, F. H., "Orderly structure in jet turbulence," *J. Fluid Mech.*, Vol. 48, 1971, pp. 547–591.

[33]Ffowcs Williams, J. E. and Kempton, A. J., "The noise from the large-scale structure of a jet," *Journal of Fluid Mechanics*, Vol. 84, 1978, pp. 673–694.

[34]Crighton, D. and Huerre, P., "Shear-layer pressure fluctuations and superdirective acoustic sources," *Journal of Fluid Mechanics*, Vol. 220, No. 1, 1990, pp. 355–368.

[35]Cavalieri, A. V. G., Jordan, P., Colonius, T., and Gervais, Y., "Axisymmetric superdirectivity in subsonic jets," *Journal of Fluid Mechanics*, Vol. 704, 2012, pp. 388–420.